

# Micro-Calcification Detection in Digital Tomosynthesis Mammography

Frederick W. Wheeler<sup>a</sup>, A. G. Amitha Perera<sup>a</sup>, Bernhard E. Claus<sup>a</sup>,  
Serge L. Muller<sup>b</sup>, Gero Peters<sup>b</sup> and John P. Kaufhold<sup>c</sup>

<sup>a</sup>GE Global Research, Niskayuna, NY, USA;

<sup>b</sup>GE Healthcare X-ray, Buc, France;

<sup>c</sup>SAIC, McLean, VA, USA

## ABSTRACT

A novel technique for the detection and enhancement of microcalcifications in digital tomosynthesis mammography (DTM) is presented. In this method, the DTM projection images are used directly, instead of using a 3D reconstruction. Calcification residual images are computed for each of the projection images. Calcification detection is then performed over 3D space, based on the values of the calcification residual images at projection points for each 3D point under test. The quantum, electronic, and tissue noise variance at each pixel in each of the calcification residuals is incorporated into the detection algorithm. The 3D calcification detection algorithm finds a minimum variance estimate of calcification attenuation present in 3D space based on the signal and variance of the calcification residual images at the corresponding points in the projection images. The method effectively detects calcifications in 3D in a way that both ameliorates the difficulties of joint tissue/microcalcification tomosynthetic reconstruction (streak artifacts, etc.) and exploits the well understood image properties of microcalcifications as they appear in 2D mammograms. In this method, 3D reconstruction and calcification detection and enhancement are effectively combined to create a calcification detection specific reconstruction. Motivation and details of the technique and statistical results for DTM data are provided.

**Keywords:** Computer-Aided Diagnosis, Image Enhancement, Limited-Angle Reconstruction, X-ray and CT, Mammography

## 1. INTRODUCTION

Breast cancer is the most prevalent type of cancer in women, with an annual incidence rate of 37 per 100,000 in the world.<sup>1</sup> Early detection is the most effective means of reducing the mortality rate, with screening—primarily x-ray mammography—reducing the rate about 30%. However, the specificity of mammography is low, with 70–80% of detected abnormalities being benign.<sup>2</sup>

A major cause for the low specificity is that current standard mammography practice uses 2D projection images, and diagnosis is confounded by superposition of parenchymal tissue. Such superposition can mimic a lesion in the projection image, leading to a false positive, or mask a lesion, giving a false negative.

Digital Tomosynthesis Mammography (DTM) is a limited-angle tomography system which alleviates the tissue superposition problem. DTM takes several x-ray projection images of the breast under compression using different x-ray source locations, as depicted in Fig. 1. A tomographic reconstruction is then performed to produce a three-dimensional (3D) image of the breast tissue.<sup>3, 4, 5, 6</sup> DTM systems have been developed and are now becoming available for clinical testing for screening and diagnosis applications.

Microcalcifications, along with masses and architectural distortions, are important indicators of breast cancer. Radiologists visually search mammograms for clusters of microcalcifications with particular shapes and arrangements. A microcalcification finding can by itself indicate breast cancer and lead to an interventional procedure. While the primary benefit of DTM is expected to be in mass detection because the superposition problem will be largely eliminated, 3D localization of calcifications—and analysis of their clusters—will also be greatly improved.

---

Send correspondence to: Frederick W. Wheeler (wheeler@crd.ge.com)

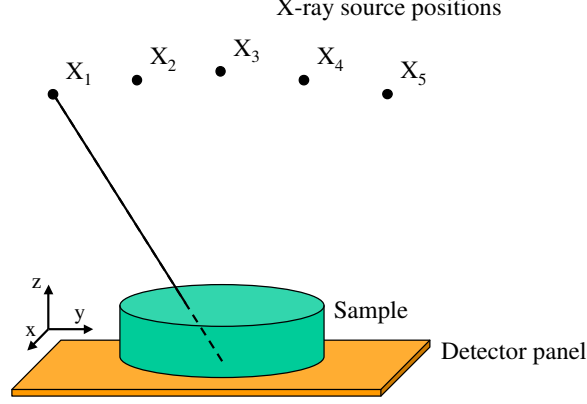


**Figure 1.** In tomosynthesis imaging, the detector panel and sample remain fixed as a series of projection images are collected, each with a different x-ray source position.

Microcalcifications of greatest clinical interest are very small and have a high x-ray attenuation coefficient relative to the rest of the breast tissue. At typical mammogram x-ray energies, the attenuation of calcifications is approximately 11 times that of fibroglandular tissue and 14 times that of adipose tissue.<sup>7</sup> Important microcalcifications generally have a diameter in the 100–500 $\mu\text{m}$  range, which is roughly the size of the point spread function of a modern digital detector. On a film mammogram, a magnifying glass is often required to see microcalcifications. Calcifications can also be much larger, but very large calcifications usually indicate benign conditions.

Complementing recent DTM computer-aided detection development focused on masses,<sup>8, 9, 10, 11, 12</sup> the work presented here is concerned with the detection and enhancement of microcalcifications in DTM. Specifically, our motivation is the detection of small microcalcifications (about 100 $\mu\text{m}$  in size) that are at the threshold of detectability for the system.<sup>13</sup> Calcifications that are considerably larger are of course easier to detect, and should be detected and labeled by a complete system, but that is not our present concern.

Total patient dose in DTM is comparable to current two-view (CC, MLO) mammography, but is distributed over many projections. Therefore, each individual projection gets a much smaller dose and thus has a lower SNR, making it difficult to apply standard 2D approaches to each projection independently. In contrast, our approach uses all the available information simultaneously. While processing will begin in the 2D projections, no hard decisions are made based on individual projection image data.

## 2. OVERVIEW

It is of course important to fully utilize the 3D information available from medical tomosynthesis images. For a person, this is naturally done by viewing a 3D reconstruction directly. For image analysis algorithms, it is not necessarily the case that operating on the 3D reconstruction data makes best use of the information available. Some 3D image analysis processing may perform better by simultaneously using all of the projection images directly instead of operating on a 3D reconstruction.

The approach we take is to work directly with the projections instead of a 3D reconstruction, for several reasons. It is in the projections where we have the more accurate noise model and observer model of microcalcifications and can still account for variations in the sensitivity and noise for each pixel. A 3D DTM reconstruction has limitations; it may have streak artifacts and is not isotropic in resolution, having better spatial resolution in the X and Y dimensions than in the Z dimension (perpendicular to the detector). By using the projections directly as the observations for this detection problem we avoid having to model the distortions and limitations of the 3D DTM reconstruction. Of course, all of the information in the 3D reconstruction is present in the projections; by working directly from the projections we still fully utilize all available information. In following

this approach, the resulting detector essentially combines calcification detection with reconstruction. For small microcalcifications, we believe that this is the most efficient approach to detection.

An effective approach to the detection of microcalcifications in a conventional 2D mammogram is to smooth the log-counts image to form an estimate of the parenchymal tissue without microcalcifications. Linear low-pass smoothing or median filtering has little effect on the signal from the parenchymal tissue, but reduces noise and reduces or eliminates microcalcifications from the image. The difference between the original and the smoothed mammogram is the calcification residual and is an estimate of the additional linear attenuation due to microcalcifications for which the noise is readily modeled.<sup>14, 15, 16</sup>

We generalize this approach for DTM. However, instead of using a 3D reconstruction we generalize specifically for limited-angle DTM by combining information directly from the projections themselves using statistical modeling. Calcification residual images are computed for each projection, along with a noise estimate for each pixel in the residuals. Detection of calcification at a 3D location is accomplished by combining evidence of calcification at the corresponding projection locations in each of the residual images. The result is a 3D DTM microcalcification detection algorithm that combines reconstruction and detection and fully utilizes all available information from the scan.

In the following, as a notational convention, we will use a prime ( $A'$ ) to indicate an image without gain correction, lower-case ( $a$ ) to indicate an image in the log-counts domain, and a hat ( $\hat{a}$ ) to denote a noisy measurement or estimate.

### 3. SIGNAL MODEL

We use a monochromatic image formation model where the uncorrected intensity at each detector pixel is given by

$$C'(i, j) = S(i, j)P_0(i, j) \exp \left[ \int_{p \in \text{path}} -\mu(x, y, z) dp \right] \quad (1)$$

where  $C'(i, j)$  is proportional to the amount of charge (counts) at the individual pixel at coordinate  $(i, j)$ ,  $\mu(x, y, z)$  is the x-ray attenuation coefficient of the sample at each point in space between the detector and the x-ray source, and the integral is over the path,  $p$ , which describes the trajectory of x-rays from the source to the detector pixel location.  $P_0(i, j)$  is the energy incident on the sample, whose amplitude is proportional to the mAs setting.  $P_0(i, j)$  accounts for the anode heel effect and other angular and propagation distance variations of the system.  $S(i, j)$  is the sensitivity of each detector pixel. The attenuation coefficients  $\mu(x, y, z)$  span a wide range, which includes attenuation due to parenchymal tissue, glandular (fibrous) tissue, fatty tissue, calcium salts, and air. This signal model does not account for the x-ray spot size, scatter, the detector PSF, or polychromatic x-ray energy.

In tomosynthesis imaging, several projections are taken of the same sample, with the x-ray source in different positions, as shown in Fig. 1. These images are denoted by  $C'_n(i, j)$ , with source positions denoted by  $X_n$ , where  $n = 1, \dots, N$ .

Variations in pixel sensitivity are corrected with

$$C_n(i, j) = G(i, j)C'_n(i, j) \quad (2)$$

where  $G(i, j)$  is a calibration gain map and  $G(i, j) \approx 1/(S(i, j)P_0(i, j))$ . In this application, as in reconstruction, these corrected projections,  $C_n(i, j)$ , are used by subsequent processing steps. The calibration procedure generally also corrects bad pixels (where  $S(i, j) = 0$ ) and corrects for detector bias with a calibration dark map, but there is no need to consider those features of the system here.

The log-count domain, defined by

$$y_n(i, j) = -\log(G(i, j)C'_n(i, j)) \quad (3)$$

is the attenuation coefficient-thickness product domain where tissue signal components are additive and linear signal processing methods are justified. The analysis here is in the log-count domain to facilitate linear combination of signals derived from the projections, as is typical in tomography.

#### 4. NOISE MODEL

The most important aspect of tomography that we will exploit here is that any  $(x, y, z)$  location is observed  $N$  times, each time along a different propagation path. The noise for each of the  $N$  observations is different because the x-ray attenuation along each path is different, affecting quantum noise. This will be more pronounced as the projections are taken at larger angles, and if the dose per projection varies. Also, each path hits a different detector pixel with a different sensitivity,  $S(i, j)$ . Properly modeling and accounting for the variation in noise is a motivation for this approach.

We use a noise model with three components: quantum noise, electronic noise, and structure noise. Quantum noise and electronic noise are easily modeled by well understood physical principles, while the structure noise model for fine fibroglandular tissue is more phenomenological. That is, we consider very fine fibroglandular structure that interferes with calcification detection to be a noise source and model it based on its appearance. We will elaborate on structure noise in Section 6.

Let  $\hat{C}'_n(i, j)$  denote the uncorrected intensity measurements actually read from the detector, a noisy estimate of the theoretical noise free measurement  $C'_n(i, j)$ . The uncorrected projections  $\hat{C}'_n(i, j)$  are corrupted by quantum noise and additive electronic noise

$$\hat{C}'_n(i, j) = Q_n(i, j) + N_n(i, j) \quad (4)$$

By the strict Poisson noise model, the quantum noise component  $Q_n(i, j)$  is a Poisson random variable with  $E\{Q_n(i, j)\} = C'_n(i, j)$  and variance  $\sigma_Q^2 = C'_n(i, j)$ . In practice we can model  $Q_n(i, j)$  as Gaussian with the same mean and variance since the Poisson distribution converges to the Gaussian distribution with a high number of counts.<sup>17</sup> The electronic noise component  $N_n(i, j)$  is Gaussian with zero mean and variance  $\sigma_N^2$ . There are a variety of scaling, averaging, and other system effects that cause  $\sigma_Q^2$  to be proportional to, but not equal to,  $C'_n(i, j)$ . So, we will model  $\hat{C}'_n(i, j)$  as Gaussian with expected value  $E\{\hat{C}'_n(i, j)\} = C'_n(i, j)$ , and variance

$$\sigma_{C'}^2 = \alpha^C C'_n(i, j) + \beta^C \quad (5)$$

that has a component proportional to  $C'_n(i, j)$  for the quantum noise and a constant component for the electronic noise. We know the noise variance will have this form but we leave the parameters  $\alpha^C$  and  $\beta^C$  to be determined from the data. The superscript  $C$  indicates that these are the parameters for the counts-domain projections, which will change below when we move to the log-counts domain. The noise parameters will be estimated from the data, and are fixed for a set of projections.

A first-order approximation to the logarithm and a low-noise assumption leads to the approximation that the noise in the log-count domain is also Gaussian with variance

$$\sigma_y^2 \approx \frac{\alpha C'_n(i, j) + \beta}{(C'_n(i, j))^2} = \frac{\alpha}{C'_n(i, j)} + \frac{\beta}{(C'_n(i, j))^2} \quad (6)$$

This approximation is derived using a first-order Taylor series approximation to the logarithm in (3). Because of the sign change and gain correction scaling by  $G(i, j)$ , parameters  $\alpha$  and  $\beta$  in (6) are not equivalent to parameters  $\alpha^C$  and  $\beta^C$ , respectively, in (5). It is perhaps counterintuitive, but note that the application of the logarithm makes the otherwise simply additive electronic noise component now have a variance dependent on the signal level.

#### 5. CALCIFICATION RESIDUAL SIGNAL

In our image formation model, and in reality, the presence of a microcalcification has a simple and isolated affect—a small region of a projection has an elevated attenuation. We will use an observer model of calcifications on projection images in the log-count domain. We will estimate the non-calcification tissue signal and subtract it from each projection, creating a calcification residual image that contains the calcification signal plus noise we will model.

The log-count domain signal is modeled as two parts, separating the calcification contribution from the rest

$$y_n(i, j) = b_n(i, j) + c_n(i, j) \quad (7)$$

Here  $b_n(i, j)$  is the fat and glandular tissue signal, and  $c_n(i, j)$  is the additional attenuation of calcification on this path. Our goal is now to estimate  $c_n(i, j)$ . The noisy estimate of  $y_n(i, j)$ , determined from (3) using  $\hat{C}'_n(i, j)$ , that we actually acquire is modeled as

$$\hat{y}_n(i, j) = b_n(i, j) + c_n(i, j) + r_n(i, j) \quad (8)$$

where  $r_n(i, j)$  is the quantum and electronic noise in the corrected log-count domain. Noise signal  $r_n(i, j)$  is Gaussian, zero mean, uncorrelated between pixels and projection images, and has variance as modeled by (6). Because the calcifications are so small we ignore the reduction in  $b_n(i, j)$  that comes from their presence by displacement of other tissue and let  $c_n(i, j)$  represent additional attenuation due to calcification.

We form an estimate  $\hat{b}_n(i, j)$  of  $b_n(i, j)$  by smoothing the signal  $\hat{y}_n(i, j)$ . The desired effect is to maintain the slowly varying signal  $b_n(i, j)$ , while removing small calcifications and reducing the noise, yielding  $\hat{b}_n(i, j) \approx b_n(i, j)$ . A 2D Gaussian smoothing kernel ( $\sigma \approx 500\mu\text{m}$ , 5 pixels) is used here, though non-linear filters such as a median filter or a gradient directed filter are suitable as well, especially to help smoothing over calcification and noise without smoothing over fine linear structures. The system's PSF, if significant, could be incorporated into this smoothing operation, though that is not done here. The calcification residual signal is then computed with

$$\hat{c}_n(i, j) = \hat{y}_n(i, j) - \hat{b}_n(i, j) \quad (9)$$

and is a noisy estimate of the additional attenuation due to microcalcification.

Some amount of very fine fibroglandular tissue structure in  $b_n(i, j)$  will be filtered out when estimating  $\hat{b}_n(i, j)$ . We refer to the difference between  $\hat{b}_n(i, j)$  and  $b_n(i, j)$  as structure noise and model it below as zero-mean Gaussian in the log-count domain with variance estimated from the data. This structure noise is simply the portion of the very fine non-calcification image detail that ends up in the calcification residual.

The calcification residual is the difference between the projection and the low-pass filtered projection. This is effectively a high-pass filter, but it is important to keep the low-pass operation separate, conceptually and in practice, because it is our low noise estimate of the non-calcification signal from which we get our pixel flux estimate and the calcification residual noise estimate depends on the pixel flux estimate.

## 6. CALCIFICATION RESIDUAL NOISE

We now develop the noise model for the calcification residual signal  $\hat{c}_n(i, j)$ . First, our estimate of the tissue signal  $\hat{b}_n(i, j)$  is converted back to the counts domain and the gain map correction is removed with

$$B'_n(i, j) = \exp(-\hat{b}_n(i, j))/G(i, j) \quad (10)$$

Then  $B'_n(i, j)$  serves as an estimate of flux  $C'_n(i, j)$  that determines the amount of noise at a pixel, assuming that no calcification is present. Note that  $\hat{C}'_n(i, j)$  is less desirable as an estimate of the flux because it is more noisy. Also, this flux estimate involves smoothing  $\hat{y}_n(i, j)$  in the log-counts domain as opposed to, for example, smoothing  $G(i, j)\hat{C}'_n(i, j)$  in the count domain. Now,  $B'_n(i, j)$  is used in the noise model, and we assume that all the quantum and electronic noise from  $\hat{y}_n(i, j)$  ends up in  $\hat{c}_n(i, j)$  and thus  $\hat{c}_n(i, j)$  has mean  $c_n(i, j)$  and variance of the form

$$\sigma_c^2 = \frac{\alpha B'_n(i, j) + \beta}{(B'_n(i, j))^2} + \gamma \quad (11)$$

where  $\alpha$  is the parameter for the quantum noise component,  $\beta$  is the parameter for the electronic noise component and  $\gamma$  is a new parameter for the structure noise component. This is the variance of the calcification residual in the log-counts domain, when no calcification is present.

The noise model parameters  $\alpha$ ,  $\beta$  and  $\gamma$  are fixed over the set of projections and are estimated from the actual projections and the calibration gain map by fitting the noise model to variances computed from the data. Projection pixels are binned according to the flux estimate  $B'_n(i, j)$ . Pixels that are not some distance within the tissue mask (described below) are not used. The variance of the calcification residual  $\hat{c}_n(i, j)$  is then computed

for each bin. Parameters  $\alpha$ ,  $\beta$  and  $\gamma$  are found that best map the flux estimate midpoint to the computed calcification residual variance for each bin.

Studies of calcification residual noise statistics for conventional mammograms indicate that the quantum noise is significantly greater than electronic or structure noise.<sup>13, 18</sup> With the dose budget spread over more projections in DTM quantum noise becomes even more dominant, relative to the other noise sources. The significance of quantum noise is further elevated in areas of dense tissue where counts will be reduced. This is an important motivation for our approach since quantum noise will be different for each detector pixel and the technique presented here is designed to exploit this. It is also important to note that, since we are working in the log-counts domain, even the electronic noise is dependent on counts because of the nature of the logarithm, as shown in (6), and will be different for each detector pixel. We have found that, for a typical scan, over all projections and pixels in the log-count domain, the total noise standard deviation, from (11) with estimated parameter values, can vary by a factor of 4, though this result is preliminary.

## 7. THREE-DIMENSIONAL CALCIFICATION DETECTION

The calcification detection is applied to each point on a 3D grid independently. So, we can describe the algorithm in terms of how it is applied for a single point  $(x, y, z)$ . Let  $(i, j)$  be the 2D coordinates of the projection of the 3D point  $(x, y, z)$  onto the detector plane for projection  $n$ , so,  $\hat{c}_n(i, j)$  is the calcification residual for the projection of this 3D point, and has variance  $\sigma_{c,n}^2(i, j)$  from (11). For notational convenience we denote these values as  $\hat{c}_n$  and  $\sigma_{c,n}^2$ .

We are attempting to detect the presence of calcification at  $(x, y, z)$ . Assuming an approximately spherical shape, the presence of a calcification will increase  $\hat{c}_n$  for each projection approximately the same amount,  $D$ , proportional to the size of the calcification. With  $N$  measurements of the same unknown parameter we use the minimum variance estimator<sup>19</sup>

$$\hat{D} = \sum_{n=1}^N \frac{1}{\sigma_{c,n}^2} \hat{c}_n \bigg/ \sum_{n=1}^N \frac{1}{\sigma_{c,n}^2} \quad \text{var}\{\hat{D}\} = 1 \bigg/ \sum_{n=1}^N \frac{1}{\sigma_{c,n}^2} \quad (12)$$

When done over a volume this is essentially shift and add reconstruction of the calcification residual signal, weighted by the inverse of its variance. More sophisticated reconstruction techniques might be useful at this stage as well. There are options as to how to use  $\hat{D}$ . A hard detection decision can be made by comparing  $\hat{D}$  to a threshold. The variance of  $\hat{D}$  could be used to set that threshold or could be used by subsequent processing. However, we will instead use  $\hat{D}$ , computed at the same 3D locations and denoted  $\hat{D}(x, y, z)$ , to enhance a conventional reconstruction.

If the calcification residual variance were ignored, then the calcification attenuation estimator and variance would be

$$\hat{D} = \frac{1}{N} \sum_{n=1}^N \hat{c}_n \quad \text{var}\{\hat{D}\} = \frac{1}{N^2} \sum_{n=1}^N \sigma_{c,n}^2 \quad (13)$$

The more the calcification residual variances,  $\sigma_{c,n}^2$ , change across the projections the greater the benefit of the minimum variance estimator.

The calcification residual is computed only for 3D points that lie within the tissue volume. To determine when this is the case, a *tissue mask* is computed for each tomographic projection image. The tissue mask has value 1 for pixels corresponding to breast tissue and 0 otherwise. A 3D point is considered inside the tissue if it projects to a pixel on the tissue mask with value 1 for each projection image.

The tissue mask is automatically determined from corrected projection images by thresholding and mathematical morphology. In the first stage, the mask is initially defined by those pixels with intensity between two empirically determined thresholds. This mask is morphologically opened to remove small strings of isolated pixels, and then closed to cover small gaps. Both the open and close operators use a disk with radius  $500\mu\text{m}$  (5 pixels). In the majority of the cases, the resulting mask consists of the breast tissue being isolated as the largest component in the mask. For the results below the tissue mask was further eroded by 2.5mm to avoid spurious responses at the skin-line. This parameter can of course be set to a clinically appropriate value.

## 8. RESULTS

In this section we show the results of applying the calcification detection reconstruction algorithm to real tomographic data. Figure 2 shows an unenhanced generalized filtered backprojection<sup>5</sup> reconstructed slice alongside the reconstructed slice enhanced by addition of the thresholded and scaled calcification detection output. Figure 4 shows an enlarged section of the reconstructed slice in Fig. 2, the corresponding calcification detection signal  $\hat{D}(x, y, z)$ , and the enhanced reconstructed slice.

To produce the enhanced slice, a threshold value is subtracted from the calcification detection signal  $\hat{D}(x, y, z)$ , negative values are set to zero and the result is scaled and added to the original reconstruction for the purpose of drawing attention to the calcification. This enhances small calcifications, as is clearly seen.

For these preliminary results the threshold is selected manually. On the  $300 \times 400$  pixel section in Fig. 4, 67 pixels (0.055%) were modified by the enhancement. This makes small calcifications much more prominent while still primarily showing the ordinary reconstruction.

Figures 3 and 5 show a corresponding set of images for a different patient. In this example more non-calcification fine linear structures are being enhanced. It is expected that subsequent shape-based filtering will mitigate this.

Fig. 6 shows two histograms. One is of the pixel values of the reconstruction and the other is of the corresponding calcification detection signal, for the region shown in Fig. 4. In each histogram, calcifications result in sparse outliers to the extreme right of the primary mode. For the original reconstruction, the peak value is 7.1 standard deviations from the mean, and for the calcification detection signal, the peak value is 14.9 standard deviations from the mean. Subsequent processing will benefit from this significantly enhanced separation of calcification signal and noise. It is this signal to noise ratio that directly affects the performance of calcification detection, whether automatic or by a radiologist.

This example shows some calcifications that are visible but faint in the reconstruction being detected clearly. A presumption of this approach is that by processing and combining the projections we might better detect calcifications that are indistinguishable from noise in the full reconstruction. Absent a large reconstructed DTM dataset with pixel-level ground-truth, which is expensive and tedious to produce, the best illustration of the merit of this 3D approach is its effectiveness on faint microcalcifications. The performance of our method on the faint microcalcifications indicated in Fig. 6 is evidence that we are indeed selectively and substantially increasing contrast in a graded way even on faint microcalcifications and not on similar fibroglandular tissue.

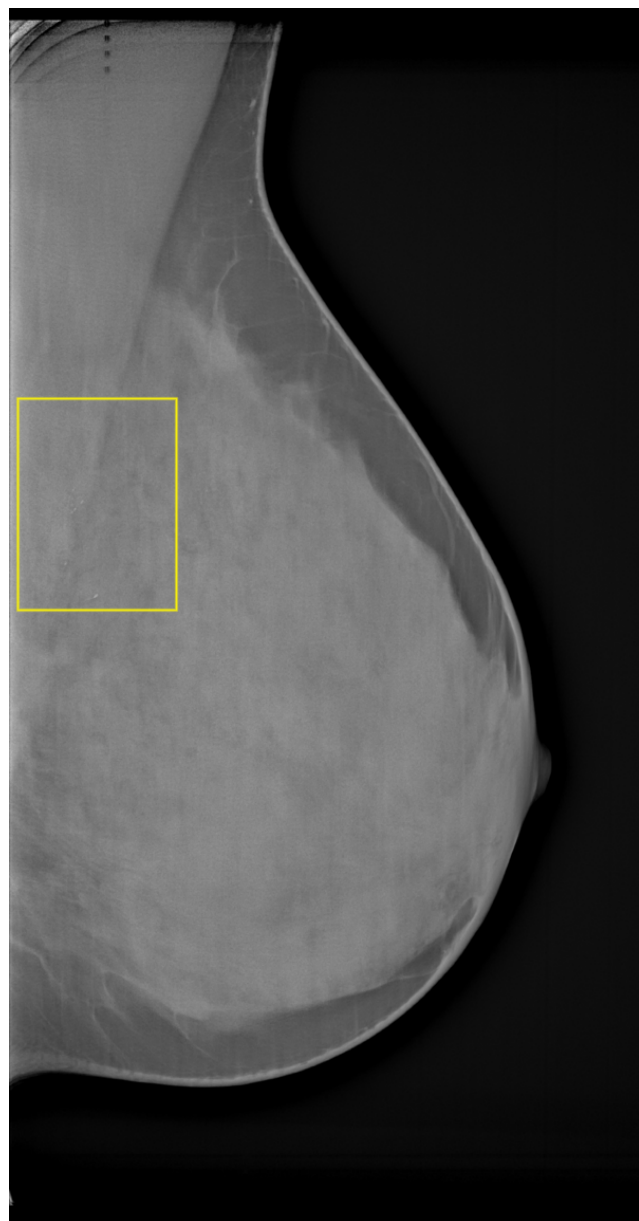
## 9. CONCLUSIONS AND DISCUSSION

We have presented a technique for the detection and enhancement of small microcalcifications from a digital tomosynthesis projection image set. Our focus has been on noise modeling in the projection images and using that noise model appropriately in the detection process, effectively creating a 3D detector that directly and simultaneously utilizes the information in all of the projections. We feel this an appropriate approach for detection of small microcalcifications, since their effect on the projections is easily modeled. Not presented here, but essential parts of a larger system, are calcification shape and distribution analysis to improve detection and classification.<sup>20, 21</sup>

Useful further work in this area includes more thoroughly validating the noise model on real and phantom data and extending the noise model for both the presence and absence of calcification for classical hypothesis testing.

Working directly on the 2D projection images is not solely for the sake of adapting existing 2D algorithms to this modality. This is still inherently a 3D algorithm, as the reconstruction and detection are effectively combined. However, working directly on the 2D projection images allows for a more accurate image formation and noise model.

Working directly with the projection images makes sense for small microcalcifications in DTM. However, this is a special case, due in part to the fact that small microcalcifications have a simple signature in each projection. For larger calcifications, or for masses, accurate simultaneous modeling in the projections is more difficult. Further, when detecting larger and more complicated shapes, the benefits of precise pixel-level noise modeling will diminish.



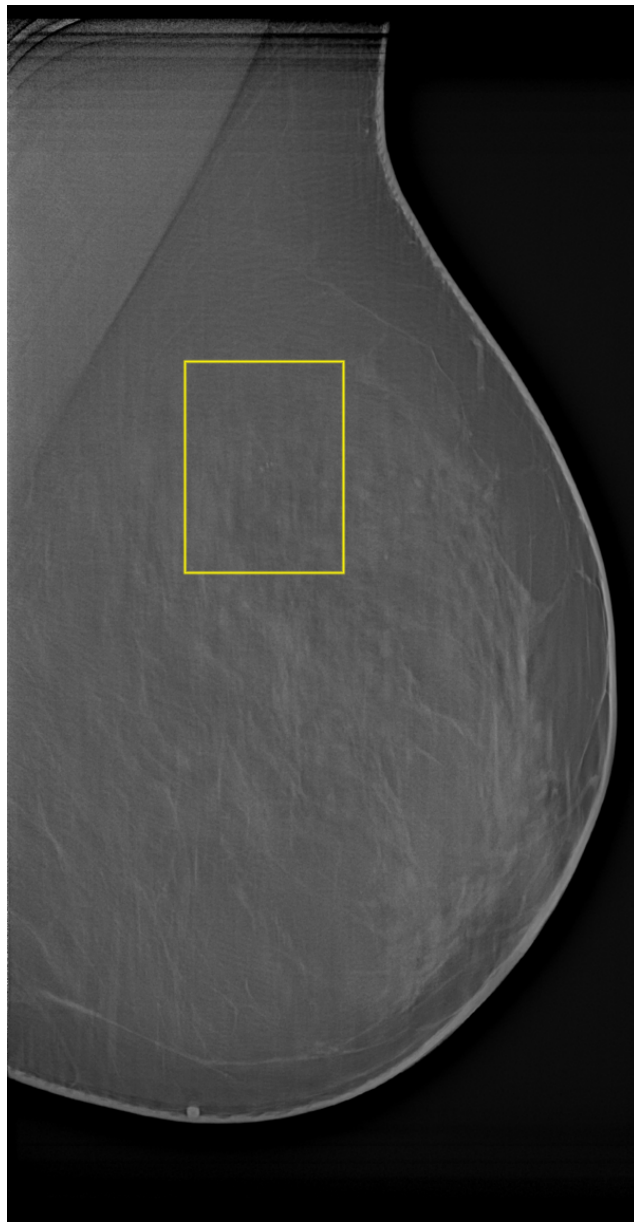
Reconstruction



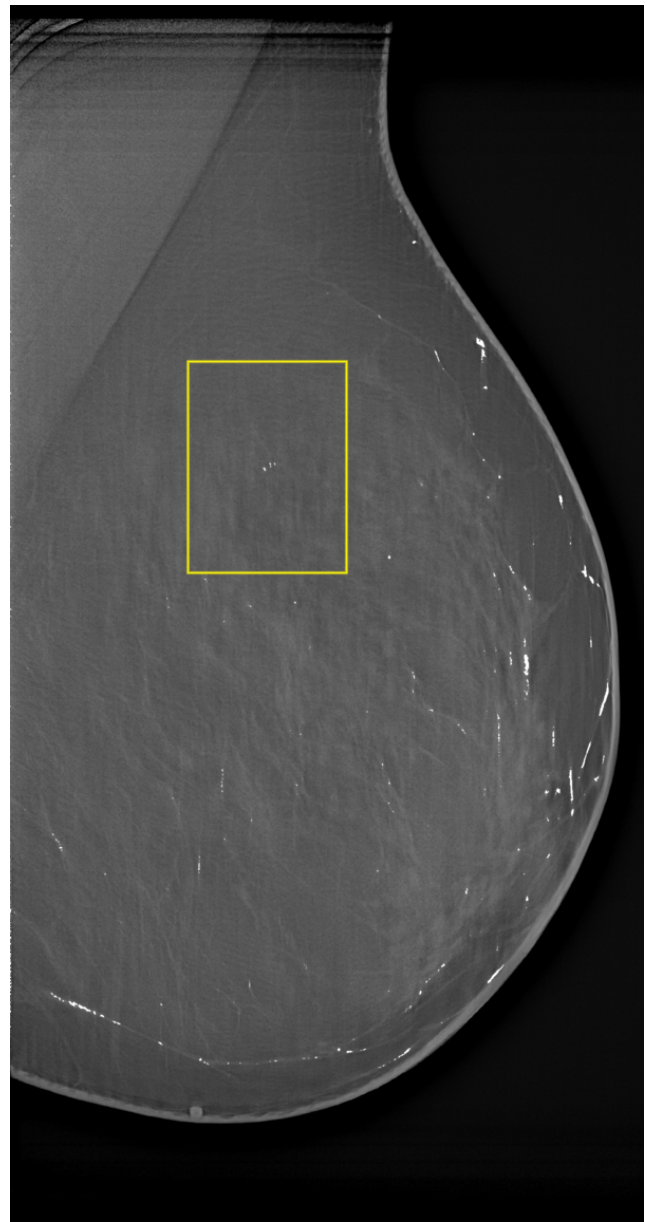
Enhanced Reconstruction

**Figure 2.** A 120mm×230.4mm (1200×2304 pixels) reconstruction slice and the enhanced reconstruction. The small enhancement details are clearly visible in the electronic version of this document. The rectangle encloses the region detailed in Fig. 4. (Tomographic projection data provided courtesy of Dr. D. Kopans, Massachusetts General Hospital.)





Reconstruction



Enhanced Reconstruction

**Figure 3.** A  $120\text{mm} \times 230.4\text{mm}$  ( $1200 \times 2304$  pixels) reconstruction slice and the enhanced reconstruction. The small enhancement details are clearly visible in the electronic version of this document. Fine linear structures are also enhanced; it is expected that subsequent shape-based filtering will mitigate this. The rectangle encloses the region detailed in Fig. 5. (Tomographic projection data provided courtesy of Dr. D. Kopans, Massachusetts General Hospital.)

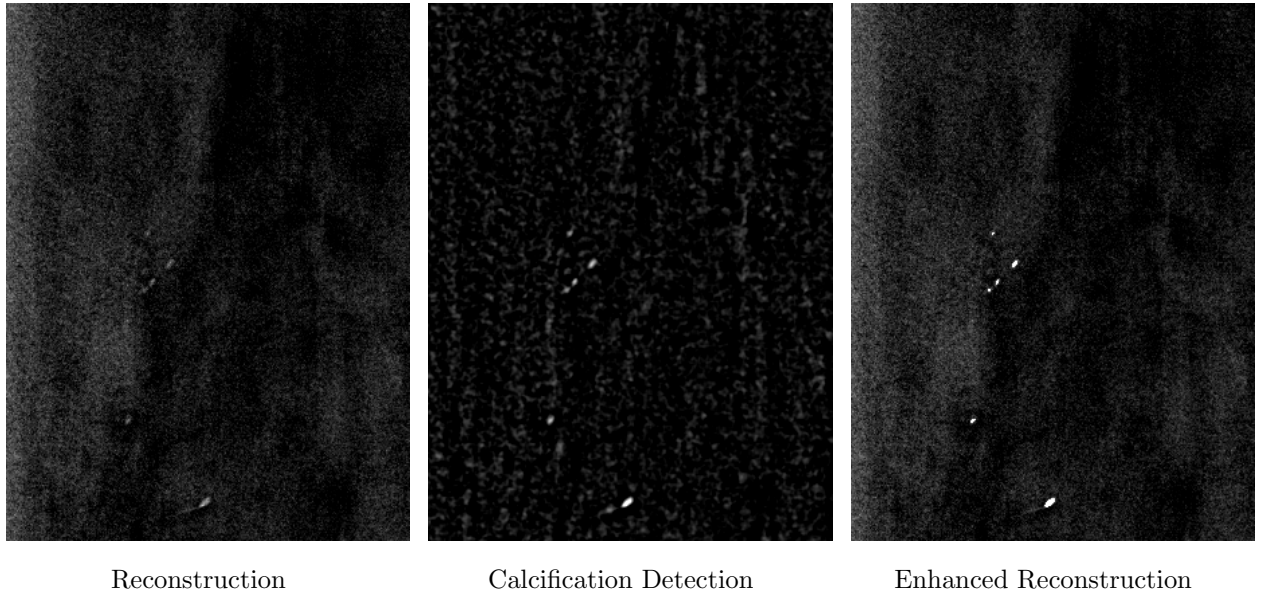


**Figure 4.** A 30mm×40mm (300×400 pixels) selected region of the reconstruction slice in Fig. 2, the corresponding calcification detection signal and the enhanced reconstruction. Some very faint calcifications are being enhanced. (Tomographic projection data provided courtesy of Dr. D. Kopans, Massachusetts General Hospital.)

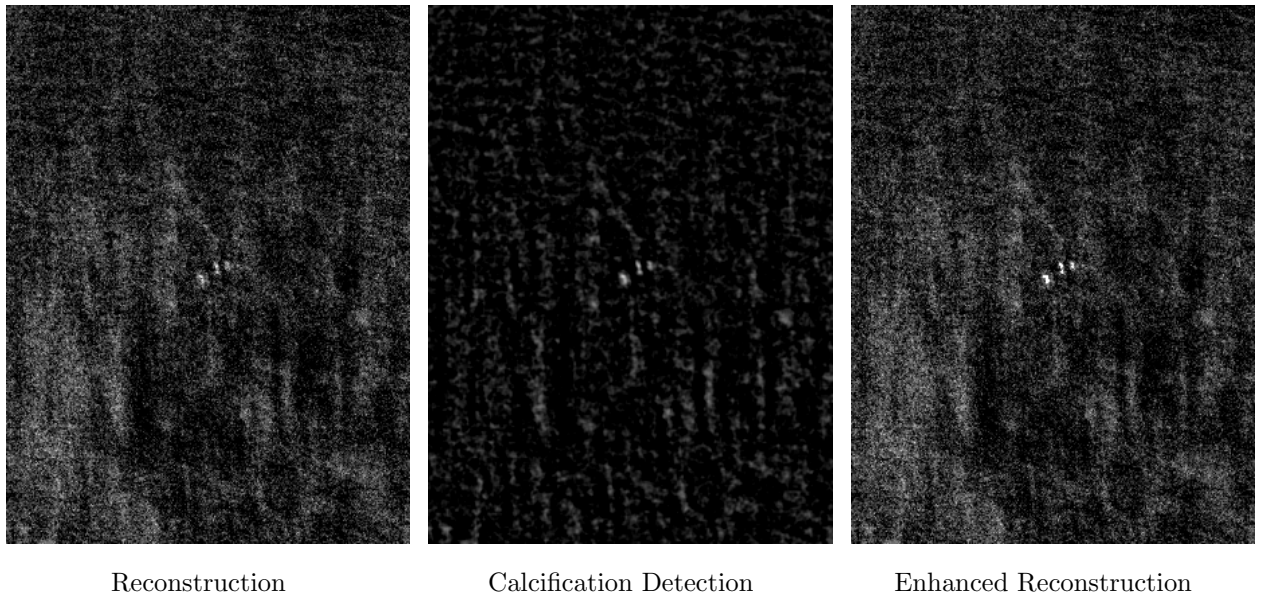


**Figure 5.** A 30mm×40mm (300×400 pixels) selected region of the reconstruction slice in Fig. 3, the corresponding calcification detection signal and the enhanced reconstruction. Some very faint calcifications are being enhanced. (Tomographic projection data provided courtesy of Dr. D. Kopans, Massachusetts General Hospital.)

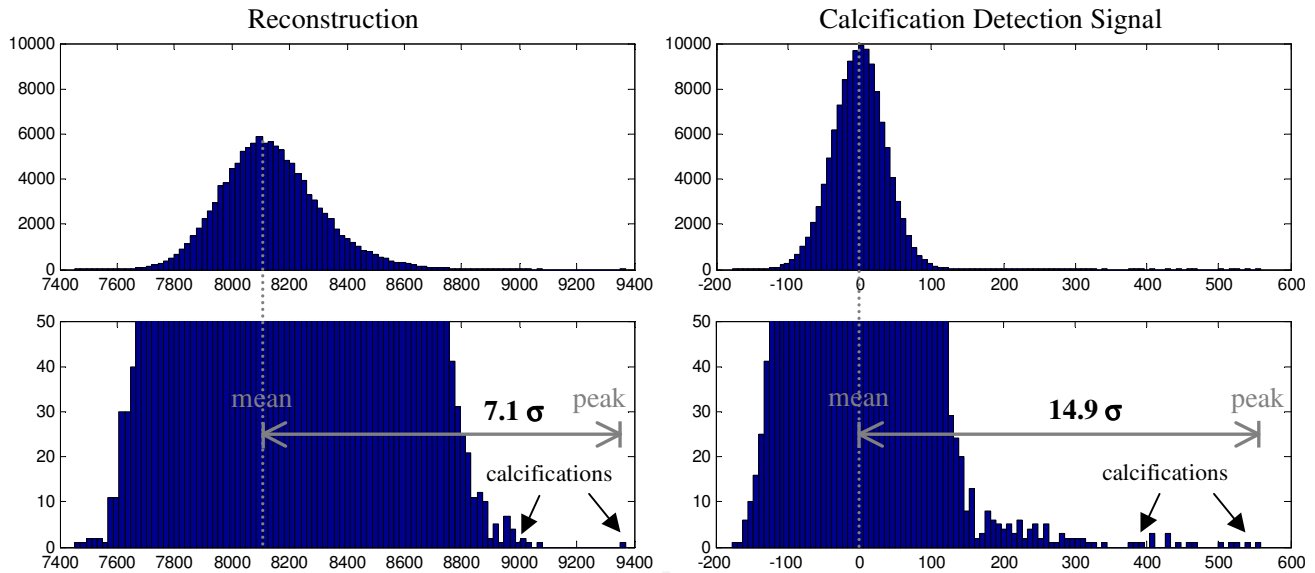


**Figure 6.** Histograms of the pixel values from the selected region of the ordinary reconstruction and also of the calcification detection signal. Each histogram is also shown zoomed in so the sparse calcification outliers are visible.

## REFERENCES

1. D. M. Parkin, F. Bray, J. Ferlay, and P. Pisani, "Global cancer statistics, 2002," *CA Cancer J Clin.* **55**, pp. 74–108, Mar–Apr 2005.
2. D. B. Kopans, *Breast Imaging*, Lippincott Williams & Wilkins, 2nd ed., 1997.
3. J. T. Dobbins III and D. J. Godfrey, "Digital x-ray tomosynthesis: current state of the art and clinical potential," *Physics in Medicine and Biology* **48**, pp. R65–R106, 2003.
4. B. Claus and J. W. Eberhard, "A new method for 3D reconstruction in digital tomosynthesis," in *Proc. of SPIE, Medical Imaging and Image Processing* **4684**, (San Diego, CA), 2002.
5. B. E. H. Claus, J. W. Eberhard, J. A. Thomas, C. E. Galbo, W. P. Pakenas, and S. L. Muller, "Preference study of reconstructed image quality in mammographic tomosynthesis," in *Proceedings of the 6th International Workshop on Digital Mammography*, H.-O. Peitgen, ed., Springer, (Bremen, Germany), June 2003.
6. T. Wu, A. Stewart, M. Stanton, T. McCauley, W. Phillips, D. B. Kopans, R. H. Moore, J. W. Eberhard, B. Opsahl-Ong, L. Niklason, and M. B. Williams, "Tomographic mammography using a limited number of low-dose cone-beam projection images," *Medical Physics* **30**, pp. 365–380, March 2003.
7. M. J. Berger, J. H. Hubbell, S. M. Seltzer, J. S. Coursey, and D. S. Zucker, *XCOM: Photon Cross Sections Database: NIST Standard Reference Database 8 (XGAM) - NBSIR 87-3597*, NIST, 1999.
8. H. Chan, J. Wei, B. Sahiner, E. Rafferty, T. Wu, M. Roubidoux, R. Moore, D. Kopans, L. Hadjiiski, and M. Helvie, "Computerized detection of masses on digital tomosynthesis mammograms: A preliminary study," in *Proceedings of the 7th International Workshop on Digital Mammography*, pp. 199–202, June 2004.
9. H.-P. Chan, J. Wei, B. Sahiner, E. Rafferty, T. Wu, and J. Ge, "Computer-aided detection on digital breast tomosynthesis (DBT) mammograms: Comparison of two approaches," in *RSNA*, (Chicago, IL), November 2004.
10. I. Reiser, R. M. Nishikawa, M. L. Giger, T. Wu, E. Rafferty, R. Moore, and D. B. Kopans, "Computerized detection of mass lesions in a series of projection images for digital breast tomosynthesis—preliminary results," in *Proceedings of the 7th International Workshop on Digital Mammography*, pp. 578–583, June 2004.
11. I. Reiser, R. Nishikawa, M. Giger, E. Rafferty, D. Kopans, and R. Moore, "Computerized mass detection for digital breast tomosynthesis directly from the projection images," in *RSNA*, (Chicago, IL), November 2004.

12. I. Reiser, R. M. Nishikawa, M. L. Giger, T. Wu, E. Rafferty, R. H. Moore, and D. B. Kopans, "Computerized detection of mass lesions in digital breast tomosynthesis images using two- and three dimensional radial gradient index segmentation," *Technology in Cancer Research & Treatment* **3**, pp. 437–442, October 2004.
13. A. E. Burgess, "Effect of detector element size on signal detectability in digital mammography," in *Proc. of SPIE, Medical Imaging and Image Processing* **5745**, (San Diego, CA), 2005.
14. N. Karssemeijer, "Stochastic model for automated detection of calcifications in digital mammograms," *Image and Vision Computing* **10**, pp. 369–375, July/August 1992.
15. W. J. H. Veldkamp and N. Karssemeijer, "Normalization of local contrast in mammograms," *IEEE Trans. on Medical Imaging* **19**, pp. 731–738, July 2000.
16. K. J. McLoughlin, P. J. Bones, and N. Karssemeijer, "Noise equalization for detection of microcalcification clusters in direct digital mammogram images," *IEEE Trans. on Medical Imaging* **23**, pp. 313–320, March 2004.
17. W. H. Press, S. A. Teukolsky, W. T. Vetterling, and B. P. Flannery, *Numerical Recipes in C: The Art of Scientific Computing*, Cambridge University Press, Cambridge, England, 2nd ed., 1992.
18. J. Kaufhold, "A sensor fusion approach to dual energy x-ray imaging for mammography: Glandular tissue composition estimation and microcalcification detection/thickness estimation," GE Global Research Center TISCAT Technical Report, Technical Information Series 2004GRC124, GE Global Research Center, Niskayuna, NY, April 2004.
19. S. M. Kay, *Fundamentals of Statistical Signal Processing: Estimation Theory*, vol. 1, Prentice Hall, 1993.
20. A. Rick, S. Bothorel, B. Bouchon-Meunier, S. Muller, and M. Rifqi, *Fuzzy Techniques in Image Processing*, vol. 52 of *Studies in Fuzziness and Soft Computing*, ch. Fuzzy Techniques in Mammographic Image Processing. Springer-Verlag Telos, June 2000.
21. G. Peters, S. Muller, S. Bernard, R. Iordache, F. Wheeler, and I. Bloch, "Reconstruction-independent 3D CAD for calcification detection in digital breast tomosynthesis using fuzzy particles," in *Proceedings of the 10th Iberoamerican Congress on Pattern Recognition (CIARP)*, November 2005.